

# Tunable Dopants with Intrinsic Counterion Separation Reveal the Effects of Electron Affinity on Dopant Intercalation and Free Carrier Production in Sequentially Doped Conjugated Polymer Films

Taylor J. Aubry, K. J. Winchell, Charlene Z. Salamat, Victoria M. Basile, Jeffrey R. Lindemuth, Julia M. Stauber, Jonathan C. Axtell, Rebecca M. Kubena, Minh D. Phan, Matthew J. Bird, Alexander M. Spokoyny,\* Sarah H. Tolbert,\* and Benjamin J. Schwartz\*

Carrier mobility in doped conjugated polymers is limited by Coulomb interactions with dopant counterions. This complicates studying the effect of the dopant's oxidation potential on carrier generation because different dopants have different Coulomb interactions with polarons on the polymer backbone. Here, dodecaborane (DDB)-based dopants are used, which electrostatically shield counterions from carriers and have tunable redox potentials at constant size and shape. DDB dopants produce mobile carriers due to spatial separation of the counterion, and those with greater energetic offsets produce more carriers. Neutron reflectometry indicates that dopant infiltration into conjugated polymer films is redox-potential-driven. Remarkably, X-ray scattering shows that despite their large 2-nm size, DDBs intercalate into the crystalline polymer lamellae like small molecules, indicating that this is the preferred location for dopants of any size. These findings elucidate why doping conjugated polymers usually produces integer, rather than partial charge transfer: dopant counterions effectively intercalate into the lamellae, far from the polarons on the polymer backbone. Finally, it is shown that the IR spectrum provides a simple way to determine polaron mobility. Overall, higher oxidation potentials lead to higher doping efficiencies, with values reaching 100% for driving forces sufficient to dope poorly crystalline regions of the film.

## 1. Introduction

Modern electronics rely heavily on semiconductor technology for everything from transistors and light-emitting diodes (LEDs) to renewable-power-generating photovoltaic and thermoelectric devices.<sup>[1]</sup> One of the key properties of semiconductors is that they can be doped to improve conductivity or adjust interfacial band alignment via tuning of the Fermi level.<sup>[2]</sup> Conjugated polymers have emerged as potential alternatives to inorganic semiconductors that have the advantages of being low-cost, lightweight, solution processable, earth-abundant and compatible with flexible substrates.<sup>[3,4]</sup> Despite these promising benefits, implementation of semiconducting polymer materials in practical technologies has lagged mainly because their intrinsic electrical properties are inferior to their inorganic counterparts.

Unlike inorganic semiconductors, where the packing structure is largely

Dr. T. J. Aubry, K. J. Winchell, C. Z. Salamat, V. M. Basile, Dr. J. M. Stauber, Dr. J. C. Axtell, R. M. Kubena, Prof. A. M. Spokoyny, Prof. S. H. Tolbert, Prof. B. J. Schwartz  
Department of Chemistry and Biochemistry  
University of California, Los Angeles  
Los Angeles, CA 90095-1569, USA  
E-mail: spokoyny@chem.ucla.edu; tolbert@chem.ucla.edu; schwartz@chem.ucla.edu

Dr. J. R. Lindemuth  
Lake Shore Cryotronics  
Westerville, OH 43082, USA

Dr. M. D. Phan  
Neutron Scattering Division  
Oak Ridge National Laboratory  
Oak Ridge, TN 37831, USA

Dr. M. J. Bird  
Chemistry Department  
Brookhaven National Laboratory  
Upton, NY 11973, USA

Prof. A. M. Spokoyny, Prof. S. H. Tolbert, Prof. B. J. Schwartz  
California NanoSystems Institute  
University of California, Los Angeles  
Los Angeles, CA 90095-7227, USA

Prof. S. H. Tolbert  
Department of Materials Science and Engineering  
University of California, Los Angeles  
Los Angeles, CA 90095-1595, USA

 The ORCID identification number(s) for the author(s) of this article can be found under <https://doi.org/10.1002/adfm.202001800>.

DOI: 10.1002/adfm.202001800

unaffected by substitutional or interstitial dopant atoms, doping of conjugated polymers causes significant disruption to the polymer morphology. Moreover, the relatively low dielectric constant of conjugated polymers typically results in strong Coulomb binding of the charge carriers with the counterions that balance the charge, so that the doped charge carriers can be strongly localized due to strong Coulomb interactions.<sup>[5–9]</sup> Understanding the relationship between the chemical nature of the dopant, the way the dopant counterions interact with the carriers on the doped polymer backbone, and the polymer morphology is crucial for developing high-performance polymer-based electronics.

Multiple methods for doping polymer thin films exist, including electrical gate doping and electrochemical doping,<sup>[10–12]</sup> but chemical doping is the only method that produces equilibrium carriers via a ground-state charge transfer process without the application of an external potential. Molecular or chemical doping of conjugated polymers involves the addition of an electron donor (reducing agent) or an electron acceptor (oxidizing agent) for *n*- or *p*-type doping, respectively.<sup>[13]</sup> Due to electron trapping, *p*-type doping of conjugated polymers is the most common,<sup>[14,15]</sup> in which a high electron affinity (EA) oxidizing agent removes electrons from the polymer's highest occupied molecular orbital (HOMO), producing conductive holes.

The traditional approach for chemical doping of conjugated polymers is to simply mix the polymer and dopant in solution and then directly cast a doped film. Unfortunately, the resulting doped material is highly insoluble, so the charged species that form upon doping crash out of solution. This leads to poor film quality and thus limits the types of measurements and applications possible with doped films.<sup>[16,17]</sup> To overcome film quality issues at high doping levels, new processing methods have applied the dopant to a pre-cast film of the undoped semiconducting polymer. Such methods include vapor-phase deposition<sup>[18–24]</sup> or solution-phase infiltration via a second spin-coating step in which a semiorthogonal solvent that swells but does not dissolve the polymer is used.<sup>[5–7,16,17,21–27]</sup> These sequential processing (SqP) methods enable preservation of the original undoped polymer film morphology and allow for conductivity measurements on cm length scales as well as for AC-Hall effect measurements<sup>[28,29]</sup> that provide a way to determine the doped carrier concentration and mobility in these materials.<sup>[6,16,30–32]</sup>

A dominant idea in the literature has been that highly crystalline polymer films are necessary to achieve good charge transport properties, with many molecular doping papers focusing on improving polymer solid state order.<sup>[5,16,20–24,31]</sup> In a previous work, we showed that we could use solution SqP to control the crystallinity of doped conjugated polymer films.<sup>[5]</sup> For the widely used poly(3-hexylthiophene-2,5-diyl) (P3HT) and 2,3,5,6-tetrafluoro-7,7,8,8-tetracyanoquinodimethane (F<sub>4</sub>TCNQ) materials combination, we indeed found higher carrier mobilities in more crystalline films. More recently, however, we employed a substituted icosahedral dodecaborane (DDB) cluster as a novel dopant and obtained high carrier mobilities for P3HT ( $\geq 0.1 \text{ cm}^2 \text{ V}^{-1} \text{ s}^{-1}$ ) in doped films that were very poorly crystalline.<sup>[6]</sup> This shows that crystallinity is not necessary for good charge transport, as has also been argued elsewhere.<sup>[33,34]</sup>

The key reason that the DDB dopants can produce mobile charge carriers without crystalline order is because DDB

clusters tend to stabilize electron density on their central core.<sup>[6,35,36]</sup> This means that for our bulky  $\approx 2$ -nm diameter DDB dopant, the negative charge of the counterion effectively lies at least  $\approx 1$  nm from any carrier, so that Coulomb binding of the carrier and counterion is significantly reduced, regardless of how crystalline the polymer is. Moreover, we found that the doping efficiency (number of free carriers produced per dopant molecule) for our DDB-doped P3HT films was close to 100%.<sup>[6]</sup> This stands in sharp contrast to the doping efficiency of F<sub>4</sub>TCNQ-doped P3HT, which is only 5–10%.<sup>[37,38]</sup>

Given that crystallinity is not required, why does it appear to be necessary for good carrier mobility in conjugated polymers doped with molecular dopants such as F<sub>4</sub>TCNQ? In general, polymers are semicrystalline materials and with two characteristic crystalline features: a lamellar spacing, determined by the length of the side chains, and a  $\pi$ -stacking distance. There is a great deal of structural work showing that F<sub>4</sub>TCNQ, the most commonly used doping agent, as well as other dopants, tend to infiltrate into the polymer lamellae.<sup>[5,21,25–27,30,39–44]</sup> For F<sub>4</sub>TCNQ-doped P3HT, the counterions in the lamellae sit at a distance of 6–8 Å from the polymer backbone.<sup>[5,22,23,25]</sup> Once the crystallites are filled, any additional dopant occupies the amorphous regions of the film, where the counterion can get significantly closer to the carriers on the polymer backbone,<sup>[5]</sup> resulting in an increase in the number of Coulombically trapped carriers at higher doping concentrations.<sup>[45]</sup> Thus, the key reason that high crystallinity is important for good conductivity with small-molecule dopants like F<sub>4</sub>TCNQ is that crystallinity helps reduce Coulombic interactions by keeping the dopant counterions farther from the polymer backbone where the polaron resides.<sup>[6]</sup>

Despite this progress in our understanding of molecular doping, one question that has not been sufficiently addressed is the effect of dopant redox potential on the production of carriers. Doping efficiency is expected to increase with the energetic offset between the polymer HOMO and dopant LUMO.<sup>[2,46,47]</sup> Yet, to date, few papers have been able to pin down exactly how the electronic offset affects doping efficiency largely because of the problems inherent in disentangling structural from electronic effects. In previous studies, either only slight tuning of the dopant oxidation potential was possible (while maintaining an energetic offset large enough to dope),<sup>[21,48,49]</sup> or significant structural changes of the dopant were necessary to more dramatically tune the oxidation potential,<sup>[6,46,49,50]</sup> which in turn changes the Coulomb interaction between the counterion and doped carriers. In other studies, quantification of the charge carrier properties (mobility and carrier density) was not carried out or was not the main focus of the study.<sup>[50,51]</sup>

In this paper, we address the effect of electronic offset on doping efficiency by employing a series of DDB dopants for which the redox potential is tuned over nearly 1 V without changing the overall size or shape of the dopant and thus without changing the Coulomb interaction between the carriers and the counterions. We find that not only is the redox potential of the dopant critical for the production of free carriers, it also is necessary to drive the dopant into the film and into the polymer crystallites. We show that there is a simple way to estimate carrier mobility from the measured IR spectrum of doped P3HT and that the mobilities of the carriers created by different DDB dopants are similar. Moreover, just like what has been

found for other small-molecule<sup>[5,20,21,25–27,30,39,41–44]</sup> and some larger dopants,<sup>[40]</sup> the  $\approx 2$ -nm diameter DDBs prefer to reside in the lamellar region of P3HT crystallites. The fact that many dopants intercalate in the polymer crystallite lamellae explains why partial charge-transfer complexes, which commonly occur in charge-transfer salts where there is direct contact between the donor and acceptor, are relatively rare in polymeric systems: In polymeric systems, dopants preferentially reside in the lamellar regions where they are not close enough to the polymer backbone to form partial-charge transfer complexes. Overall, our work shows that with careful control of the dopant size, shape and redox potential, the doping efficiency and carrier mobility can be readily understood.

## 2. Results and Discussion

The main reason that it has been difficult to study how the energetic offset between the polymer HOMO and dopant LUMO affects doping efficiency and carrier mobility is that changing the dopant redox potential has required modifying the dopant's molecular structure, which in turn changes the Coulomb interaction between the polarons and the dopant counterions. In this work, we take advantage of DDB clusters that have similar size and shape and whose redox potentials can be controllably tuned via their substituents.<sup>[36,52,53]</sup> The clusters have an icosahedral dodecaborane core with a substituent on each boron atom in the form  $B_{12}(OCH_2R)_{12}$ , where R is a functionalized aryl group

(see Figure 1a for core structure and Figure 1c for R-group substituents). The redox potential of the cluster varies roughly linearly with the Hammett parameter of the chosen R-group,<sup>[54]</sup> providing a straightforward way to produce clusters with any desired redox potential, as shown in Figure 1b; see the Supporting Information for more details of how the redox potentials were measured. We refer to the different DDB clusters based on the structures of their substituents (Bn for unfunctionalized benzyl, *p*-F for *para*-fluoro, *p*-Br for *para*-bromo and F<sub>36</sub> and F<sub>72</sub>, where the latter two compounds are simply named after the total number of fluorines on the DDB molecules).

### 2.1. Optical and Electrical Properties of DDB-Doped P3HT Films

We focus our work on doping the semiconducting polymer P3HT, whose chemical structure is shown in Figure 1a, since it is a workhorse material for the study of chemical doping of conjugated polymers and there is a vast literature to which we can compare. We fabricated doped films via solution SqP using equimolar dopant solutions, as described in more detail in the Supporting Information; we showed in our previous work that despite the large size of the DDB-F<sub>72</sub> dopant, solution SqP allows it to intercalate throughout the depth of a pre-cast P3HT film.<sup>[6]</sup>

As a first test of the effect of redox potential on doping, we measured the absorption spectra of P3HT films doped with each of the DDB clusters whose structures are shown

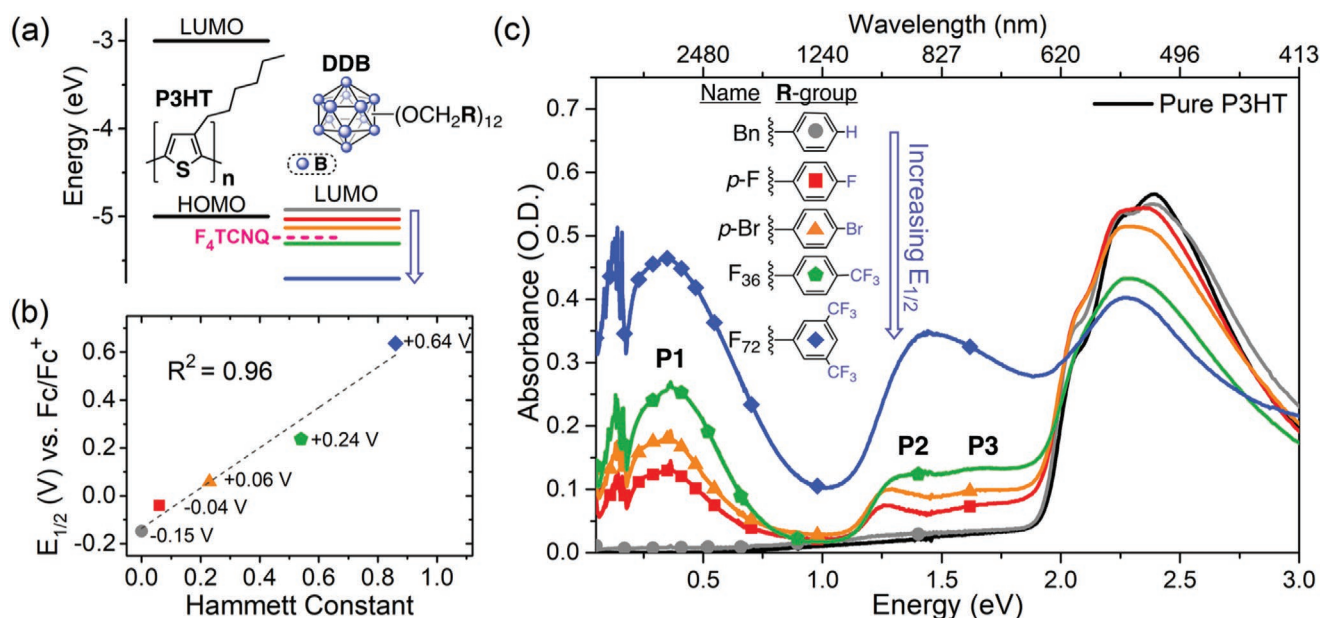


**Figure 1.** a) Chemical structures of the P3HT polymer and DDB dopants, which have an icosahedral B<sub>12</sub> core and each vertex functionalized with the R-groups shown in (c). The energy diagram depicts the relative offsets between the P3HT HOMO and dopant LUMOs. CV measurements of the DDB dopants and F<sub>4</sub>TCNQ, performed under identical conditions, are shown in Figure S1, Supporting Information. The diagram is drawn to scale based on literature values of the P3HT HOMO (-5 eV vs vacuum) and F<sub>4</sub>TCNQ LUMO (-5.2 eV vs vacuum); see Section S2, Supporting Information, for details. b) Measured  $E_{1/2}$  for DDB dopants plotted against their Hammett constant showing tunability of the DDB dopant redox potential based on the substituents' electron donating/withdrawing ability. c) UV-vis-IR spectra of 120-nm thick films of P3HT doped with 1 mM DDB via SqP, showing an increase in signature polaron peak intensities (P1 near 0.3 eV, P2 near 1.3 eV, and P3/P3' near 1.6 eV) and a bleach of the P3HT bandgap transition near 2.4 eV. The DDB anions also absorb in the  $\approx 2.4$  eV region, explaining why the apparent bleach of the P3HT absorption is less than observed with other dopants whose anion absorption lies in other regions of the spectrum.

in Figure 1. Figure 1c shows the absorption spectra of films sequentially doped with 1 mM solutions of each DDB cluster; the spectra for films doped with 0.3 mM solutions are shown in Figure S2, Supporting Information. With the exception of the DDB-Bn cluster, which has the lowest redox potential and thus is apparently unable to dope P3HT, we see that as the films are doped, the peak at 2.4 eV from the excitonic absorption of P3HT decreases, and three new absorption peaks, labelled P1, P2, and P3 in increasing order of their energy, appear near 0.3, 1.3, and 1.6 eV. These new peaks are the classic signature of the appearance of polarons.<sup>[45,55–58]</sup> Since the P1 absorption does not overlap with either the neutral polymer or dopant anion absorptions, it provides a reasonable proxy for the number of doped carriers (although we note that the P1 absorption magnitude is not cleanly linear with carrier concentration because both the polaron spectrum and cross section change with the degree of Coulomb trapping).<sup>[5,8,9,59]</sup> Thus, Figure 1 shows that the number of carriers created increases in roughly direct proportion to the redox potential of the dopant at constant dopant size.

As we will discuss in more detail in Section 2.4, as the doping concentration is increased, the P1 absorption band near 0.3 eV grows a noticeable blue shoulder. This change in shape of the P1 band indicates that there are multiple types of polarons with different degrees of Coulomb binding to their counterions. It is now well established that the position and shape of the P1 absorption band reflects the degree of delocalization of the polarons, with redder absorption corresponding to more delocalization/less Coulomb binding and vice-versa for bluer P1 absorption.<sup>[5–9,26,59–61]</sup> In previous work, we used ultrafast spectroscopy to show that for P3HT doped with F<sub>4</sub>TCNQ, the growth of the blue shoulder at higher doping concentrations was indicative of a population of trapped carriers that appears only after the polymer crystallites are full.<sup>[45]</sup> We will argue below that this picture also holds true for the DDB dopants, and that dopants in conjugated polymers preferentially occupy the lamellar regions of their crystallites, when possible. Flat, small-molecule dopants like F<sub>4</sub>TCNQ can also  $\pi$ -stack with the polymer backbone,<sup>[62–65]</sup> but this only occurs under specialized circumstances such as carefully selected processing conditions that inhibit crystallization<sup>[62–64]</sup> or employing polymers with side chains to prevent the dopant from sitting in the lamellae and forcing it into the  $\pi$ -stacks.<sup>[65]</sup> Together, all of these studies suggest that  $\pi$ -stacking of the dopant and polymer is not a kinetically easily accessible structure.

We also measured the electrical conductivity of the films whose absorption spectra are shown in Figure 1. For these measurements, we placed electrodes at the corners of a 1.5 cm  $\times$  1.5 cm square on the samples and determined the conductivity using the Van der Pauw method, which is a type of four-point-probe measurement.<sup>[66]</sup> The measured conductivities at multiple doping concentrations are given in Table S1, Supporting Information. We see that all the DDB clusters show higher conductivity at higher doping concentrations, and in concordance with the optical spectroscopy, we also see higher conductivities for clusters with higher redox potentials. For the 1 mM doped films, the conductivities are: DDB-Bn 0 S cm<sup>-1</sup>, DDB-*p*-F 0.2 S cm<sup>-1</sup>, DDB-*p*-Br 0.4 S cm<sup>-1</sup>, DDB-F<sub>36</sub> 2.3 S cm<sup>-1</sup>, and DDB-F<sub>72</sub> 12.9 S cm<sup>-1</sup>. Curiously, we find that the film thickness also increases with increasing redox potential of the

dopant, indicating that there may be more dopant in the film at higher redox potentials; this suggests that dopant infiltration is also driven by the dopant's redox potential.

## 2.2. Vertical Structure of DDB-Doped P3HT Films

Because our DDB dopants have chemically different outer surfaces, one concern is whether the amount of cluster infiltration and thus doping could be affected by these chemical differences, particularly for the highly fluorinated dopants. Indeed, there are several reports of limited vertical intercalation of large dopants into films of conjugated polymers.<sup>[40,67]</sup> Moreover, there is not a clear mechanism to describe how dopants diffuse through conjugated polymer films,<sup>[46,68,69]</sup> although we previously have shown that DDB-F<sub>72</sub> does intercalate throughout P3HT films during solution sequential processing, which relies on swelling of the polymer underlayer by a semiorthogonal solvent.<sup>[6]</sup> Thus, we employed neutron reflectometry (NR), which is a non-destructive technique, to measure the vertical distribution of our DDB dopants within the doped polymer films. The contrast between materials for NR must come from differences in their scattering length density (SLD), which is calculated from the total scattering lengths of each of the atoms in the molecular volume. The calculated SLDs for the different molecules used in this study are summarized in Table 1, which shows that there is adequate NR contrast between the DDB dopants and P3HT, even without deuteration, as the DDB dopants have a smaller H-to-heavy-atom ratio and thus a higher SLD than P3HT. This SLD contrast between DDB dopants and P3HT enables NR to resolve the dopant distribution within the polymer matrix.

The experimental neutron reflectivity patterns for 0.3 mM-DDB-doped P3HT films are shown in Figure 2a; this doping level was chosen as a balance between having a doping level high enough to have significant electrical conductivity while maintaining a low surface roughness (which increases with increased doping concentration). The data are fit using a layered model in which the thickness, SLD, and roughness of the layers are systematically varied (details in Supporting Information) and optimized until the sum of the  $\chi^2$ -values for all the points on the curve is minimized. The best-fit SLD values as a function of distance from the substrate (defined as zero Å) are shown in Figure 2b. As expected, the undoped P3HT film fits

**Table 1.** Summary of calculated neutron SLDs of pure materials and model SLD results of pure P3HT and DDB-doped P3HT films. The calculated DDB:P3HT monomer ratios extracted from the measured SLDs show increasing dopant loading with higher-redox-potential DDBs.

	Calculated SLD (pure) [10 <sup>-6</sup> Å <sup>-2</sup> ]	Measured SLD (films) [10 <sup>-6</sup> Å <sup>-2</sup> ]	DDB:P3HT monomer
P3HT	0.6	0.56	—
DDB-Bn	1.6	0.63	1:106
DDB- <i>p</i> -F	1.8	0.81	1:30
DDB- <i>p</i> -Br	1.3	0.87	1:11
DDB-F <sub>36</sub>	1.9	1.17	1:11
DDB-F <sub>72</sub>	2.0	1.43	1:7

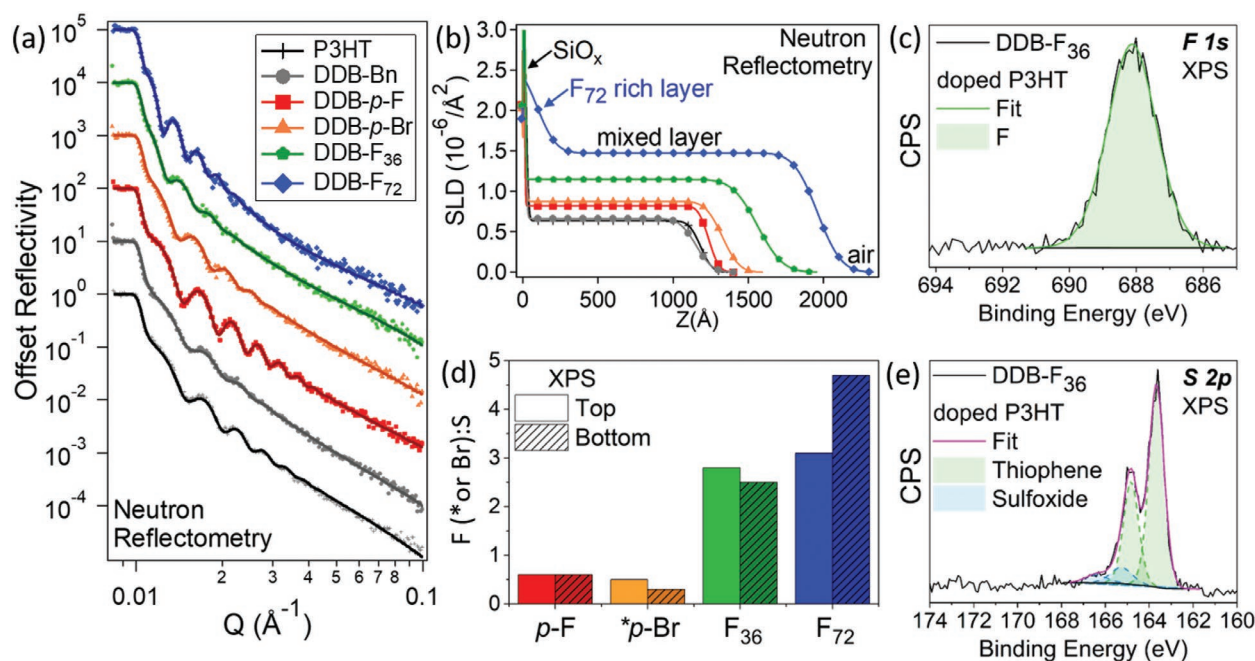


**Figure 2.** a) Raw neutron reflectivity (NR) data for pure P3HT and P3HT doped with the different DDBs via SqP (symbols) and model fits to the data (darkened curves). b) SLD depth profiles obtained from fitting the data in (a) showing the  $\text{SiO}_x$  substrate layer at 0 Å followed by the active layer before reaching the air interface. The SLD profiles show that the film thickness increases with dopant redox potential and that there is nearly uniform DDB dopant infiltration throughout the film. c) XPS-determined fluorine-to-sulfur (\*or bromine-to-sulfur for DDB-Br) ratios at the top and bottom surfaces of the DDB-doped P3HT films. The values are similar for both the top and bottom, supporting the conclusion from NR that the DDB clusters penetrate throughout the film. Sample fits to the XPS data (black) are shown in (d) for the F 1s peak (yellow) and in (e) for the S 2p peaks (green, neutral S; blue, oxidized S; and pink, full S fit) for the top surface of a DDB- $\text{F}_{36}$ -doped P3HT film (black).

to two layers: substrate and a pure polymer layer with an SLD of  $0.5 \times 10^{-6} \text{ \AA}^{-2}$ . This SLD value is in good agreement with previously measured values for P3HT.<sup>[70–72]</sup> The gradual decrease in SLD at the top surface is due to the surface roughness at the film/air interface.

For P3HT films exposed to DDB-Bn, which does not dope the polymer, the data show that there is only a slight change in the active layer SLD, indicating that there is little, if any, infiltration of this molecule into the P3HT film. As the redox potential of the DDB dopants increases, however, the measured SLD of the doped active layer also increases, with values summarized in Table 1. Because the active layer SLD is simply a weighted average of the pure SLDs of P3HT and each dopant, we can use these values to determine the P3HT monomer to DDB dopant ratio for each of our doped films; see the Supporting Information for details. The calculations show clearly that increasing the dopant redox potential leads to an increase in dopant:monomer ratio in the active layer, as also summarized in Table 1. The increasing dopant:monomer ratio, and subsequent film thickness increase as more dopants are incorporated into the P3HT matrix, suggests that the charge transfer reaction that occurs upon the introduction of a redox-active dopant into the polymer films is what drives intercalation. The non-doping cluster DDB-Bn provides an excellent control for this hypothesis as it infiltrates three times less than the next-lowest redox potential dopant (DDB-*p*-F) and approximately an order of magnitude less than the other DDBs.

The NR data also demonstrate that within the active layer of the doped polymer film, the dopant is uniformly distributed in

the direction normal to the plane of the film. The only (partial) exception to this is DDB- $\text{F}_{72}$ , for which there is a small layer with a higher dopant concentration at the substrate interface at the bottom of the film. To verify the uniformity of the DDB clusters throughout the film (and the slight excess of DDB- $\text{F}_{72}$  at the bottom of the film), we also performed a series of X-ray photoelectron spectroscopy (XPS) experiments, shown in Figure 2c–e. Although XPS cannot accurately depth-profile in the same manner as NR, it can be used to measure the relative concentration of dopant at the film surfaces. We used a delamination technique, described in our previous work,<sup>[6]</sup> to access the bottom interface of each film. We determine the relative dopant concentration at each interface by comparing the measured ratio of atomic sulfur to atomic fluorine (or bromine in the case of DDB-*p*-Br) since sulfur is unique to the P3HT polymer and fluorine (or bromine) is unique to the DDB dopants. The results show that the sulfur-to-fluorine (or bromine) ratios are similar for both the top and bottom of the DDB-*p*-F-, DDB-*p*-Br-, and DDB- $\text{F}_{36}$ -doped films (Figure 2c) suggesting uniform infiltration. The data also show that DDB- $\text{F}_{72}$  indeed has a higher dopant concentration at the bottom of the film, all in excellent agreement with the SLD profiles in Figure 2b.

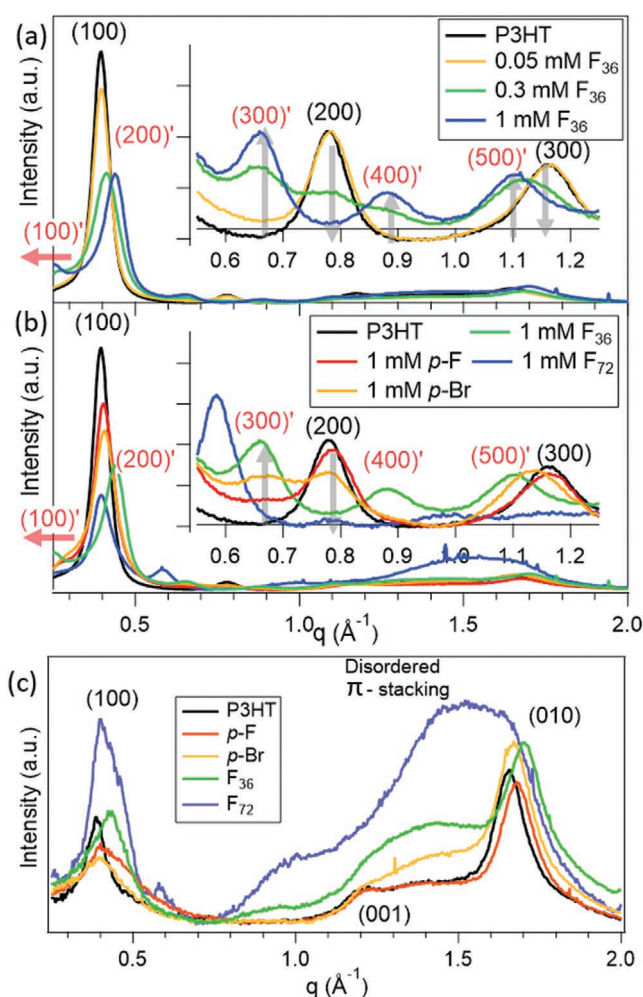
### 2.3. Local Structure of DDB-Doped P3HT Films

Although NR and XPS provide insight into the vertical distribution of dopants throughout the film and reveal redox-driven infiltration, they do not provide any information about the local

environment of the DDB dopants within the P3HT films. For a wide variety of dopants including  $F_4TCNQ$ ,  $FeCl_3$ , and polyoxometalates, among others, the counteranion resides in the lamellar region of the polymer crystallites, causing an expansion of the lattice in this direction.<sup>[5,21,25–27,30,39–44]</sup> It has been shown that this intercalation can also cause a reorientation of the crystalline unit cell, leading to a decrease in the observed  $\pi$ -stacking distance upon doping.<sup>[25–27]</sup>

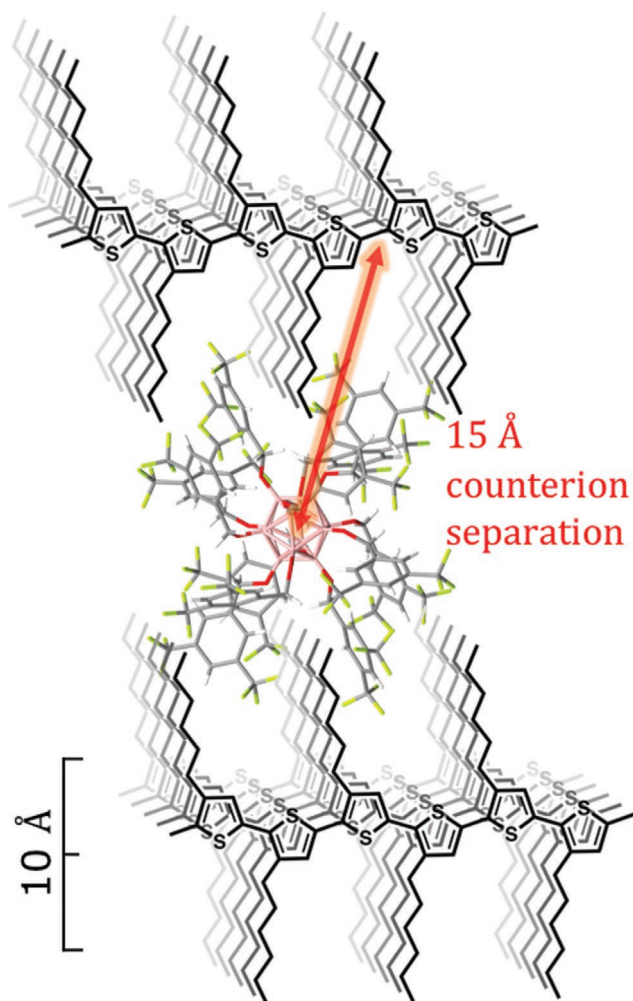
To understand the local structural effects of doping P3HT with the large DDB dopants, we performed a series of 2D grazing-incidence wide-angle X-ray scattering (GIWAXS) measurements, for which the diffractograms for all sample conditions are shown in Figure S4, Supporting Information. Figure 3a shows the progression of changes in the lamellar ( $h00$ ) out-of-plane structure of the polymer as the doping level is increased for a representative DDB. The pristine P3HT ( $100$ ) peak and corresponding overtones appear at distances representing a lamellar spacing of 16 Å. As the doping level increases, the original lamellar peaks corresponding to undoped crystalline P3HT decrease and a set of new peaks denoted as ( $h00$ )' begin to appear. At the highest doping level, the undoped P3HT ( $h00$ ) peaks have entirely disappeared, with clear new peaks appearing at 0.44, 0.66, 0.88, and 1.10  $q$ . These overtones can be indexed as ( $200$ )', ( $300$ )', ( $400$ )', and ( $500$ )', and correspond to a ( $100$ )' distance of 0.22  $q$  or 28.5 Å, indicating a highly expanded lamellar structure. (The ( $100$ )' peak is not fully visible as the beam stop blocks the low- $q$  region where it would appear). We hypothesize that the new ( $h00$ )' peaks correspond to a new phase whose general structure is shown in Figure 4. In this new phase, the DDB dopant has intercalated into the P3HT lattice in much the same way that  $F_4TCNQ$  and other small-molecule dopants do. Importantly, while the exact crystal structure of this new phase is not known, the lamellar spacing is entirely consistent with Figure 4 based on the size of the DDB dopants and the P3HT side chains (see Supporting Information for more details).

Figure 3b demonstrates that all the DDB dopants produce a similar phase change as the doping level increases. DDB- $p$ -F, which dopes P3HT only slightly, shows the beginning of this phase change, marked by an increase in scattering intensity at 0.66  $q$ , as shown in the inset of Figure 3b. For the higher-redox-potential DDB- $p$ -Br, the peaks corresponding to the new doped phase are larger relative to the intensity of the peaks of the original undoped phase. The trend continues, showing full conversion to the new phase with the higher-redox-potential DDB- $F_{36}$ . DDB- $F_{72}$  undergoes a similar phase change but to a structure with a slightly larger lamellar  $d$ -spacing, as evidenced by new ( $h00$ )' peaks at 0.40, 0.60, and 0.80 (corresponding to a ( $100$ )' peak of 0.20  $q$ , or lamellar spacing of 31 Å). All of the results are summarized in Table 2 and Figure S5, Supporting Information, which show clearly that the degree of conversion to the new phase depends directly on both the extent of doping (as evidenced by optical spectroscopy) and also on the dopant redox potential. This last conclusion is emphasized by the fact that our NR data in Table 1 showed that there are similar total amounts of DDB- $p$ -Br and DDB- $F_{36}$  molecules in the film at 0.3 mM doping concentration, yet there is significantly more conversion to new phase with DDB- $F_{36}$ . This phenomenon occurs because, in order to induce a phase transition in



**Figure 3.** a) Full integration and out-of-plane (inset) integration of the 2-D grazing-incidence wide-angle X-ray scattering (GIWAXS) of P3HT doped with DDB- $F_{36}$ . This was chosen as representative DDB doping data that demonstrates the phase change from the original undoped P3HT phase, labelled ( $h00$ ), to the lamellar-expanded doped structure, labelled ( $h00$ )'. b) Full integration and out-of-plane (inset) of the 2-D GIWAXS for P3HT doped with various DDB dopants by solution SqP at 1 mM concentration, showing the direct relationship between higher redox potential and an increased extent of phase transition to the expanded ( $h00$ )' structure c) GIWAXS in-plane integration of P3HT doped with different DDBs by solution SqP at 1 mM showing the increase in the disordered  $\pi$ -stacking region at higher doping concentrations and the slight shift of the undoped ( $010$ ) peak to higher  $q$  as doping increases.

a solid material, a critical fluctuation is required for nucleation, which should depend on the doping density. Single doping events cannot induce the required phase change alone, and in the absence of a phase transition, doping should be limited to only the surface of any crystalline domains. Thus, DDBs with higher redox potentials should be able to remove more electrons from the polymer backbone prior to the phase transition, creating a higher probability of driving the critical fluctuation that allows for nucleation of the transition to the expanded lamellar phase. DDB clusters driven into the film by the SqP process that do not undergo charge transfer also do not reside in the polymer lamellae.



**Figure 4.** To-scale representation of the proposed structure in which a DDB dopant has been incorporated into the expanded lamellar region of a P3HT crystallite. Slight interdigitation of the polymer and DDB dopant side chains is possible due to empty space in both the polymer and the dopant crystal structure. The GIWAXS data show clearly that incorporation of the dopant into the crystal structure results in this highly expanded lamellar region while largely preserving the original P3HT  $\pi$ -stacking.

For all the dramatic changes in the out-of-plane lamellar structure of the P3HT films upon doping with DDBs, the in-plane GIWAXS integrations in Figure S6, Supporting Information, show that the (010)  $\pi$ -stacking peak undergoes only slight changes, indicating that the pristine  $\pi$ -stacking morphology is largely preserved and the unit cell does not reorient as it does upon doping with  $F_4TCNQ$ .<sup>[25]</sup> We observe only a slight shift in

the (010) peak location that corresponds to smaller  $\pi$ -stacking distances, which we attribute to the delocalization of the positive charge carriers across multiple chains. This difference may stem from the fact that a change of chain tilt is required for the planar  $F_4TCNQ$  molecules to fit between the polymer side chains, but the nearly spherical DDB clusters can do nothing but push the polymer backbones apart, so chain reorientation is not energetically required. We further see that DDB doping induces an increase in the broad peak centered near  $1.4 q$ , which is associated with a disordered  $\pi$ -stacking correlation distance.<sup>[6,44]</sup> The growth of this feature increases for higher doping concentrations and with higher-redox-potential DDBs, with the most dramatic change observed for DDB- $F_{72}$ . We believe that the increase of the disordered  $\pi$ -stacking peak reflects a population of DDB anions that integrate into more disordered or amorphous regions of the doped film. The fact that this peak only appears at high doping concentrations while the (h00) peaks begin to appear at very low doping concentrations indicates that the DDB dopants preferentially reside in the crystalline lamellar regions and only occupy the more disordered regions after the crystalline regions are filled.<sup>[45]</sup> Further, the much larger increase in the intensity of this region for DDB- $F_{72}$  indicates that only this dopant has a high enough redox potential to effectively dope large amounts of the higher ionization-energy disordered regions of the film.

Interestingly, for all the DDB dopants, we see coexistence of doped and undoped phases over a broad range of dopant concentrations. This is not observed with  $F_4TCNQ$ , where minimal amounts of dopant appear to induce a phase transition in nearly all regions of the film at once,<sup>[24]</sup> and then  $F_4TCNQ$  continues to add to and “fill up” those transformed crystallites.<sup>[25]</sup> By contrast, with the DDB clusters, the structural change is so extreme that “partially filled” but expanded crystallites are more energetically favorable. Indeed, a critical doping level is likely required to induce such a dramatic phase transition in the first place. As a result, parts of the film dope to a greater extent, while some other parts remain undoped and in their original crystal structure until sufficiently high doping levels are reached. This type of two-phase coexistence is commonly seen in reactive intercalation in battery materials.<sup>[54,73,74]</sup>

#### 2.4. Degree of Polaron Localization Following Doping of P3HT with DDBs

The intercalated phase we observe from GIWAXS with DDBs in the lamellar regions of P3HT crystallites places the centers of the DDB clusters 14–15 Å from the polymer backbone, as shown in Figure 4. Since the DDB cluster anions localize

**Table 2.** Summary of calculated (100)  $d$ -spacing based on GIWAXS-measured overtones for 0.3 mM and 1 mM DDB-doped P3HT. There is a transition between the undoped and doped phases, with both phases coexisting at some doping levels. The undoped phase corresponds to the material with the initial P3HT lamellar  $d$ -spacing in the doped films.

	DDB- $p$ -F $d$ -spacing [Å]		DDB- $p$ -Br $d$ -spacing [Å]		DDB- $F_{36}$ $d$ -spacing [Å]		DDB- $F_{72}$ $d$ -spacing [Å]	
	Undoped phase	Doped phase	Undoped phase	Doped phase	Undoped phase	Doped phase	Undoped phase	Doped phase
0.3 mM DDB-doped	15.5	—	16	—	16	28	—	31
1 mM DDB-doped	15.5	—	16	28	—	28	—	31

electron density on their boron core, Gauss' law suggests that the DDB anions should behave effectively as a point charge on the center of the cluster. This means that the charges on the DDB counteranions in the crystallites are 14–15 Å from the polaron. This physical separation, which is approximately double the 6–8 Å for F<sub>4</sub>TCNQ,<sup>[5]</sup> results in minimal Coulomb binding of the polaron to the anion and thus yields highly delocalized polarons.

As mentioned above, the shape and position of the polaron IR absorption spectrum report directly on inter- and intra-chain polaron coherence as well as distance-dependant counterion Coulomb binding effects.<sup>[5–9,26,27,46,59–61]</sup> In particular, the more delocalized the polaron, the more red-shifted the main P1 absorption band (0.3–0.6 eV) and the higher the relative intensities of the so-called “IRAV” band near 0.15 eV.<sup>[5,6,8,9]</sup> In previous work from our group investigating the use of DDB-F<sub>72</sub> as a dopant, we observed a red-shifted P1 absorption and higher IRAV absorption intensity, indicating this anion was positioned to be greater than 1 nm from the polaron, something that is never seen with small-molecule dopants like F<sub>4</sub>TCNQ.<sup>[6]</sup> Indeed, a recent theoretical analysis by Ghosh et al. suggests that the DDB-F<sub>72</sub> dopant produces some of the most delocalized polarons ever observed on chemically doped P3HT.<sup>[9]</sup>

Figure 5a explores the concentration dependence of the P1 peak for DDB-F<sub>72</sub>-doped P3HT, while Figure S9a–c, Supporting Information, shows the concentration-dependent results for P3HT doped with the rest of the DDB series. For all dopants we observe a blue shoulder on the main P1 band growing in at higher dopant loadings, suggesting that the polarons created at higher doping levels are less delocalized. We observed a similar trend previously with F<sub>4</sub>TCNQ and concluded that doping at low concentrations led to incorporation into the crystalline lamellae. Not until the crystallites were full at higher doping concentrations did dopants begin to enter to the amorphous polymer regions, where the counterions can reside close to the polymer backbone.<sup>[5,45]</sup> We believe that this phenomenon—inclusion of dopants in the crystalline regions first followed by incorporation into the amorphous regions—is general to molecularly doped conjugated polymers. Indeed, the presence of the blue shoulder on the P1 band at higher doping concentrations correlates with the increase in the intensity of the disordered GIWAXS  $\pi$ -stacking peak seen near 1.4  $q$  in Figure 3c and Figure S6, Supporting Information. Both phenomena are much more pronounced for DDB clusters that have higher redox potentials.

The fact that the higher redox potential clusters have a more blue-shifted P1 spectrum provides a clue to the origin of the more localized carriers. Unlike F<sub>4</sub>TCNQ, none of the DDB clusters are capable of getting close to the polymer backbone, so Coulomb binding, as with proximal F<sub>4</sub>TCNQ, is unlikely to be responsible for the blue shoulder on the P1 absorption band. Furthermore, in our previous work,<sup>[45]</sup> we found using ultrafast spectroscopy that high doping levels result in dynamics consistent with an increase in the population of trapped polarons; we did not see evidence of polaron-polaron interactions or bipolaron formation. Instead, the less mobile carriers are likely to arise from doping-disordered regions of the polymer film, where polarons are intrinsically localized by kinks or defects in

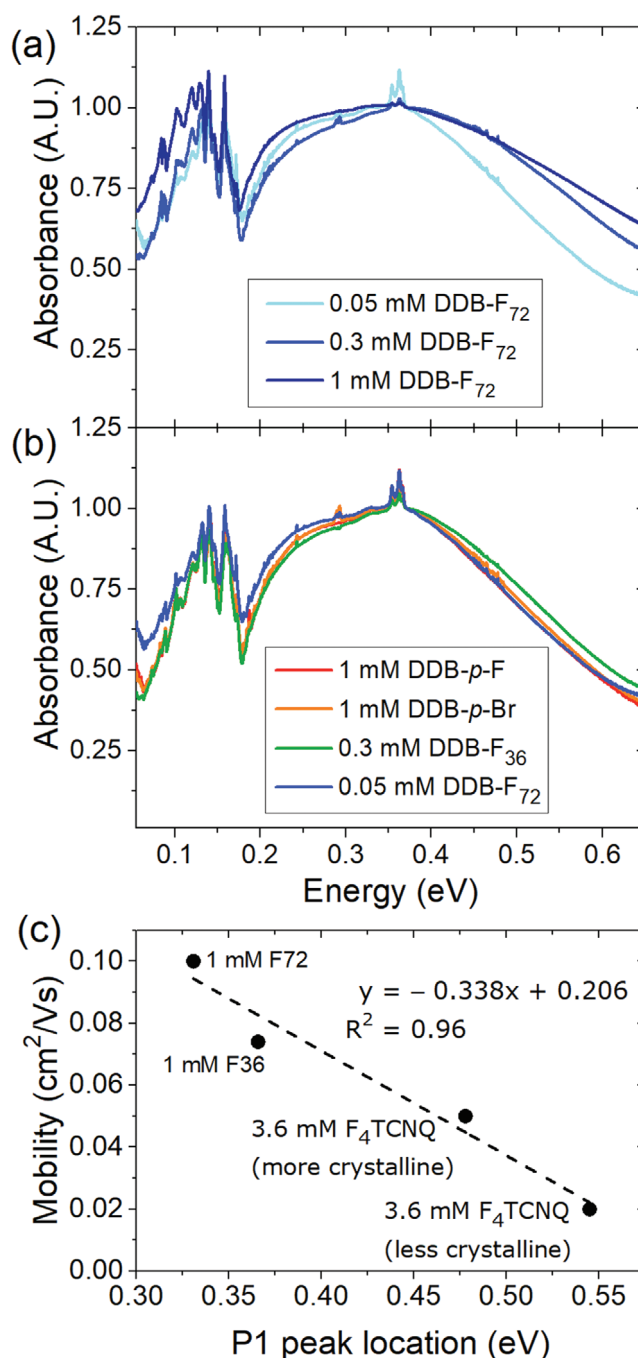


**Figure 5.** a) Normalized IR absorption of DDB-F<sub>72</sub>-doped P3HT showing the doping concentration dependence of the P1 peak location. At higher doping concentrations, we see a similar blue shift of the P1 peak for P3HT films doped with all of the DDB clusters (Figure S9a–c, Supporting Information) indicating that less mobile polarons are produced as more dopant is infiltrated into the film. b) Normalized FTIR of DDB-doped P3HT at doping-level matched concentrations (based on the GIWAXS data in Figure S5, Supporting Information) showing that the carriers produced have essentially identical anion distance and thus mobility. c) AC-Hall determined free carrier mobility versus fitted P1 absorption peak center showing a linear relationship; (Figure S9e, Supporting Information, for raw data and Figure S10a–c, Supporting Information, for fits). The F<sub>4</sub>TCNQ and DDB-F<sub>72</sub> data were taken from our previous work in refs. [5] and [6], respectively.

the polymer chain. The low mobility carriers take more energy to create, so only the DDB clusters with the greatest oxidizing potential can create such polarons, and only after all of the lower-energy redox sites have already been used up.

In agreement with this idea, for the highest doping concentration of DDB-F<sub>72</sub>, we see the most broadening of the P1 peak, which we attribute to the sample's general lack of crystallinity, yielding a wider range of configurations and therefore a wider range of polaron delocalization and coherence. The recent theoretical modeling of the P1 peak for this sample by Ghosh et al. found that the absorption spectrum was best described by two distinct counterion separations of ≈18 and ≈8 Å (in a ≈3:1 ratio).<sup>[9]</sup> The ≈18 Å distance matches well with the 15 Å distance we measure for the DDB in the lamellar spacing. The ≈8 Å distance is simply too close to represent a physical DDB-P3HT polaron distance given the size of the DDB cluster, and thus must represent the equivalent loss of mobility associated with creating carriers in the non-crystalline regions of the film. We note that even with an effective ≈8 Å spacing for the less mobile carriers at high doping concentrations, DDB-F<sub>72</sub> is still able to create more delocalized polarons than with small molecules such as F<sub>4</sub>TCNQ simply due to the size and thus Coulomb shielding of the DDB anion.

One issue when comparing the different DDB clusters to each other is that amount of cluster intercalation varies with redox potential for a given concentration, as mentioned above. Therefore, to compare polaron delocalization across the DDB cluster series, we chose concentrations that GIWAXS indicated are structurally similar, characterized by the appearance of the intercalated phase but without too much loss of the initial crystallinity. This comparison is shown in Figure 5b, which shows that all the DDB-doped P3HT polarons have nearly identical P1 lineshapes, indicating that all the DDBs are equally effective at shielding the anion from the polaron. Thus, we are indeed able to tune the electronic offset of the DDB without affecting the polaron-counterion distance. Since the polaron spectroscopy indicates that the polarons for these samples are equally delocalized, the higher conductivities we observe with the higher-redox-potential dopants must result from an increase in the number of free carriers produced, as we explore in the next section.

## 2.5. Doping Efficiency as a Function of Redox Potential at Constant Size

We saw above in our NR experiments that the number of dopants that intercalated into P3HT films following SqP increased as the redox potential of the dopant increased. This

means that it should be straightforward to determine the doping efficiency, the ratio of the number of free carriers produced to the number of dopants, as long as we can determine the free carrier density. In previous work,<sup>[5,6,16]</sup> we were able to directly measure the free carrier density using the AC-Hall effect, allowing us to obtain the carrier mobility from the measured conductivity (since conductivity is  $\sigma = ne\mu$  where  $\mu$  is the mobility,  $n$  is the carrier density and  $e$  is the elementary charge.) We found that there was a direct correlation between the position of the main P1 absorption peak, which reports on carrier delocalization, and the carrier mobility. Here, we make that correlation explicit, using data from our previous work on F<sub>4</sub>TCNQ as well as new AC-Hall measurements on DDB-F<sub>72</sub> and DDB-F<sub>36</sub>-doped P3HT films, as summarized in Figure 5c. The strong correlation means that we can use the measured P1 absorption position and electrical conductivity to provide a decent estimate of the carrier density in all of our DDB-doped films (Figures S12 and S13, Table S3, Supporting Information).

To estimate the doping efficiency, we calculated the amount of DDB in the doped films from the NR DDB:P3HT monomer ratios. Since the total amount of polymer in each film remains constant throughout the doping process, we can calculate the number of P3HT monomers using the initial film thickness (120 nm) and known P3HT film density of 1.1 g cm<sup>-2</sup><sup>[75,76]</sup> and we obtain the dopant density from the NR ratios. The results of this calculation are reported in Table 3. We then estimated the carrier concentration using the measured conductivity and the estimate of  $\mu$  given from the position of the P1 band via Figure 5c, as described in more detail in the Supporting Information. The ratio of these two numbers provide an estimate of the doping efficiency of our DDB dopants. We find that as the redox potential of the dopant is increased the doping efficiency also increases, as shown in Table 3. It is important to note that the doping efficiency, by definition, takes into account all dopant molecules, whether or not they have undergone charge transfer. Pingel and Neher estimated that with F<sub>4</sub>TCNQ, 95% of the charge transfer events led to trapped polarons, yielding a doping efficiency of roughly 5%.<sup>[37,38]</sup>

For our DDB dopants, we cannot directly probe the amount of charge transfer spectroscopically both because of the difficulty of resolving the neutral and anion peaks in the DDB-doped systems, which also strongly overlap the P3HT exciton absorption (Figures S12 and S13, Supporting Information), and because we do not know how the DDB neutral and anion absorption cross sections change between solution and film environments. However, we do know from both our AC-Hall measurements and the positions of the P1 absorption bands that the carriers produced by DDB doping are essentially all free. This means that the differences in doping efficiency we

**Table 3.** Estimated doping efficiency of DDB dopants based on the total dopant density calculated from the neutron SLD results and carrier mobilities determined either from AC-Hall effect measurements or calculated from the correlation between P1 peak locations and mobility (Figure 5c).

	Dopant density [cm <sup>-3</sup> ]	P1 center [eV]	$\mu$ [cm <sup>2</sup> V <sup>-1</sup> s <sup>-1</sup> ]	$\sigma$ [S cm <sup>-1</sup> ]	$n_{\text{est}}$ [cm <sup>-3</sup> ]	Doping efficiency [%]
DDB- <i>p</i> -F	$1.3 \times 10^{20}$	0.339	0.092	$0.016 \pm 0.003$	$1.09 \times 10^{18}$	0.8 (0.3)
DDB- <i>p</i> -Br	$3.7 \times 10^{20}$	0.328	0.095	$0.11 \pm 0.01$	$7.20 \times 10^{18}$	1.9 (0.3)
DDB-F <sub>36</sub>	$3.6 \times 10^{20}$	0.369	0.082	$0.75 \pm 0.02$	$5.74 \times 10^{19}$	16 (1)
DDB-F <sub>72</sub>	$5.3 \times 10^{20}$	0.363	0.084	$6.8 \pm 0.5$	$5.08 \times 10^{20}$	96 (10)

observe with DDB redox potential are due to differences in the number of charge transfer events. For our DDB-F<sub>36</sub> dopant, which has a redox potential that is close to F<sub>4</sub>TCNQ (higher by only ≈70 mV), we find a doping efficiency of 16%. With our highest-redox-potential dopant, DDB-F<sub>72</sub>, which has a nearly 0.5 eV greater offset than F<sub>4</sub>TCNQ, we calculate a doping efficiency of 96%, which is within the error of our previous estimate of 100%,<sup>[6]</sup> highlighting the importance of energetic offset for the generation of free carriers.

Why do higher redox-potential DDBs dope better? There may be some kinetic component, where higher redox-potential DDBs are better able to drive the phase transition needed to incorporate clusters into the polymer lamellae. In addition, the easiest place to dope in a P3HT film is in the crystallites, where the carriers can be the most delocalized and thus have a lower ionization energy. In order to dope the more amorphous regions of the films at higher doping concentrations, additional driving force to oxidize these higher-energy polymer conformations is needed. Indeed, only the high-redox-potential DDB-F<sub>72</sub> is able to dope P3HT aggregates in solution, as described in more detail in Section S8, Supporting Information.<sup>[77]</sup> Thus, the higher the redox potential of the dopant, the more ability to create carriers in different regions of a semicrystalline P3HT film. When this oxidizing power is combined with sequestration of the anion yielding minimal Coulomb trapping, it is not surprising that 100% doping efficiency can be achieved.

## 2.6. A General Picture of Chemical Doping in Conjugated Polymers

In view of previous results<sup>[5,21,25–27,30,39–44]</sup> and those that we present here for our large DDB dopants, it appears molecular dopants of all sizes, shapes, and surface energies preferentially reside in the crystalline regions of the polymer lamellae for P3HT (and likely for semiconducting polymers in general). These observations can be explained from an energetic perspective. As mentioned above, the easiest place to oxidize a conjugated polymer film is in the crystallites, where  $\pi$ -stacking of the polymer chains allows for polaron delocalization. Hamidi-Sakr et al. have shown that only a few initial F<sub>4</sub>TCNQ dopants are needed to drive the phase transition that causes reorientation and expansion of the crystalline unit cell,<sup>[25]</sup> after which additional dopants continue to occupy the crystallites until they eventually become full. The reoriented and expanded unit cell allows dopant counterions to reside in the lamellar region of the crystallites. This is because the side chains have plenty of entropy for distortion, so the free energy cost to disrupt the lamellar spacing is smaller than breaking up the polymer  $\pi$  stacks. Only once the low-energy sites are all doped and the lamellae are filled does it make sense to put dopants in the amorphous regions, where it is harder to oxidize the polymer and where more driving force for infiltration is required. Although the details of the phase transition that occurs upon incorporation of DDB clusters is different, the general phenomenon is the same. This explains why the oxidative driving force of the dopant affects the amount of dopant intercalation. If the dopant molecule does not have sufficient redox potential to oxidize the polymer crystallites, as is the case with DDB-Bn, the initial phase transition never happens,

and thus there is no way for any additional dopant to enter the polymer crystalline lattice.

Our results indicate that dopants prefer to reside in the polymer crystalline lamellae, whether they are small molecules like F<sub>4</sub>TCNQ, which can fit between the polymer side chains and expand the crystalline lamellae by only ≈10%, or large dopants, like the DDBs, which effectively double the lamellar spacing. Knowing where the dopant molecules reside is important for understanding the physics of doping because the spatial separation of the polaron and dopant counteranion is critical to determining the extent of polaron delocalization and thus the doped carrier mobility.<sup>[9,61]</sup> These considerations are especially important when dealing with low dielectric materials (such as most organic semiconductors) and therefore critical to the development of organic electronics. This is also why it is important to keep the dopant size constant when studying the effect of redox potential on doping efficiency, because dopants with different sizes will change the lamellar spacing differently and thus lie at different distances from the polymer backbone, changing the extent of Coulomb binding. The fact that dopants reside in the polymer lamellae is the best-case scenario for keeping the dopant counterion away from the polarons on the conjugated backbone, explaining why chemically doped conjugated polymers have been such a fruitful area of study.

Moreover, the fact that dopants tend to lie in the crystalline lamellae, far from the polymer's  $\pi$  system, also explains why doped conjugated polymers tend to undergo integer charge transfer rather than the partial charge transfer that is often observed with doped small molecules or oligomers.<sup>[51,78,79]</sup> Recent work has shown that under special processing conditions, there can be partial charge transfer between P3HT and dopants like F<sub>4</sub>TCNQ, and that partial charge transfer is associated with  $\pi$ -stacking of the dopant with the polymer backbone.<sup>[62,63]</sup> Creating dopant/polymer  $\pi$  stacks is clearly kinetically very challenging and potentially also thermodynamically unfavorable, which is why extreme measures must be taken to create these species. Such measures include spinning the materials from a hot solvent that keeps the polymer dissolved and prevents undoped crystallites from forming,<sup>[62,63]</sup> or synthetically modifying the polymer with branched side chains to prevent lamellar intercalation.<sup>[65]</sup> Although the thermodynamics of the situation are not fully resolved, the kinetic problem is clear. A loss of polymer  $\pi$ -stacking to create partial charge transfer complexes is energetically unfavorable, and unless dopants can fully intercalate between the polymer chains, some  $\pi$ -stacking will be lost. By contrast, when the dopants reside in the lamellar regions, the  $\pi$ -stacking in the crystalline regions is intrinsically preserved, and the loss of van der Waals interactions between dopants and the polymer side chains due to dopant vacancies has a minimal free energetic penalty. Oligomers and small molecules avoid this energetic conundrum by crystallizing directly as stacked donor/acceptor dimers, so that intimate contact and wavefunction overlap lead to partial rather than integer charge transfer.<sup>[51,78,79]</sup>

We believe that for all chemically doped conjugated polymers, the doping process is essentially identical. If the redox potential is strong enough to dope the polymer backbone with a high enough density of doping events to induce crystalline reorganization, dopants will initially enter the crystalline lamellae;

the stronger the redox potential of the dopant, the greater the ability to initiate this reorganization. Once the phase transition has occurred and the reorganized lattice has expanded in the lamellar direction, there is plenty of room to accommodate additional dopant molecules. This creates free carriers that are highly conductive because the counterions are well segregated from the polarons on the backbone, as the crystallinity of the  $\pi$  systems is largely unaffected. The mobility of these carriers will depend on the distance of the counterions from the polymer backbone and thus on the lamellar spacing, explaining why carriers created by small dopants such as  $F_4TCNQ$  are not as mobile as those created by larger dopants such as the DDBs. Once the crystalline lamellae are full, additional dopants will occupy the non-crystalline regions of the film, as evidenced by the increase in the disordered  $\pi$ -stacking peak seen by GIWAXS in Figure 3c. The amorphous regions are harder to oxidize because the polarons are less delocalized, and any polarons created in these regions have a lower mobility, as evidenced by a blue-shifted P1 absorption spectrum (Figure 5a; Figure S9a–c, Supporting Information) and slower recovery dynamics in pump-probe spectroscopy.<sup>[45]</sup> The overall doping efficiency thus depends on redox potential for two reasons: first, the potential must be high enough to cause the initial reorganization, and second, to keep doping after the crystallites are full, the redox potential must be sufficient to oxidize higher-energy sites associated with non-crystalline bends, kinks and other defects in the amorphous polymer structure.

### 3. Conclusions

In this work, we isolated the effects of electron affinity on the generation of charge carriers in chemically doped conjugated polymers by employing a unique molecular dopant system, dodecaboranes, whose redox potential can be tuned while maintaining a constant dopant size and shape. Indeed, by tuning the redox potential of the DDB and keeping the  $SqP$  doping solution concentration constant, we can tune the doping level of the sample. The higher doping levels are caused by a combination of the dopant's electron affinity and thus propensity for electron transfer and by redox-driven infiltration of the DDB dopants into the film. We characterized the vertical distribution and amount of dopants in sequentially doped films using NR. We observed mostly uniform dopant distribution throughout the film, with increasing dopant densities for higher-redox-potential clusters. Redox-driven infiltration is also corroborated by both our XPS and GIWAXS studies. Our GIWAXS characterizations show that doping leads to a new intercalated phase with a structure that has the DDB cluster sitting in the lamellar region of the polymer, very similar to the structure produced upon doping with  $F_4TCNQ$ .

The greater the infiltration of our large DDB clusters into P3HT films, of which there is more intercalation for higher-redox-potential clusters, the greater the loss of polymer crystallinity we observe. This is characterized by an observed increase in scattering from the disordered  $\pi$ -stacking peak. Despite this increased disorder, both AC-Hall and FTIR measurements indicate that the polarons are delocalized and highly mobile, highlighting the importance of anion separation to

reduce Coulomb binding. The closest distance a polaron on the P3HT backbone can get to a DDB counterion is  $\approx 1$  nm because of the built-in steric protection of the DDB core.<sup>[6]</sup> Since DDBs reside in the polymer lamellae, this leads to a typical anion–polaron distance of 1.4–1.5 nm, which corresponds well with recently reported theoretical calculations for the DDB-P3HT system in the literature.<sup>[9]</sup> The shape and location of the polaron peak in the FTIR spectra also confirm that all DDB dopants can effectively spatially separate the counterion.

Both our FTIR and AC-Hall measurements suggest that DDB doping produces virtually no trapped carriers, indicating that the different DDBs produce different doping levels because they cause different amounts of charge transfer. By combining the dopant densities we determine from NR with estimates of the carrier density from our empirically derived FTIR/AC Hall mobility relationship, we find that the DDB doping efficiency increases with redox potential. Thus, we are able to tune the number of integer charge transfer events per dopant with energetic offset. With our highest-redox-potential dopant, DDB- $F_{72}$ , we achieve a doping efficiency of 96%. The electron affinity of DDB- $F_{72}$  is what allows it to dope so efficiently because this cluster has sufficient oxidizing potential to dope both low- and high-energy P3HT conformations in the thin film.

The intercalation of dopants in polymer lamellae gives insight as to why conjugated polymers primarily undergo integer charge transfer as opposed to partial charge transfer. In charge transfer salts, the dopants can  $\pi$ -stack with the organic material being doped, whereas the general crystal structure of conjugated polymers forces dopants to reside in the lamellar regions. This means dopants are positioned further from the backbone, making partial charge transfer (in which the charge is shared between donor and acceptor) much more rare. Indeed, partial charge transfer in doped conjugated polymers is observed only in special cases,<sup>[62,63]</sup> and likely only in amorphous regions where the dopants can get closer to the polymer backbone. Therefore, the reason high crystallinity is important for good conductivity with small-molecule dopants like  $F_4TCNQ$  is that high crystallinity reduces Coulombic interactions by keeping the dopant counterions at greater distances from the polymer backbone where the polaron resides. This physical constraint is not required to keep large DDB dopants away from their polarons, which is why even though crystalline intercalated phases are observed, high conductivity is still observed even in more disordered films doped with DDBs. All of this has important implications for the creation of future dopants, which could be tailored for better anion shielding and be given an appropriate oxidizing potential, or for new dopable conjugated polymers, which could be designed with larger lamellar spacings to better isolate the dopant counterion from the polymer backbone. The fact that both large and small dopants behave in the same way provides a lot of flexibility in future dopant design, and offers great hope for the use of chemically doped conjugated polymers in a variety of electronic applications.

### Supporting Information

Supporting Information is available from the Wiley Online Library or from the author.

## Acknowledgements

T.J.A. and K.J.W. contributed equally to this work. This work was supported by the National Science Foundation under awards CHE-1608957 and CBET-1510353. Synthetic work on redox-active boron clusters at UCLA led by A.M.S. was supported as part of the Center for Synthetic Control Across Length-scales for Advancing Rechargeables (SCALAR), an Energy Frontier Research Center funded by the U.S. Department of Energy, Office of Science, Basic Energy Sciences under Award # DE-SC0019381. A portion of this work at BNL was supported by the U.S. Department of Energy, Office of Science, Office of Basic Energy Sciences, Division of Chemical Sciences, Geosciences & Biosciences under Contract DE-SC0012704. Use of the Stanford Synchrotron Radiation Lightsource, SLAC National Accelerator Laboratory was supported by the U.S. Department of Energy, Office of Science, Office of Basic Energy Sciences under contract # DE-AC02-76SF00515. Research at the Spallation Neutron Source, a DOE Office of Science User Facility operated by the Oak Ridge National Laboratory (ORNL) was sponsored by the Scientific User Facilities Division, Office of Basic Energy Sciences, U.S. Department of Energy. A portion of this research used resources at the Spallation Neutron Source, ORNL. The authors also thank Lake Shore Cryotronics for the use of their Lake Shore model 8400 series AC-Hall probe system for the Hall effect measurements.

## Conflict of Interest

The authors declare no conflict of interest.

## Keywords

counterion distance, doping efficiency, electronic offset, molecular dopants, redox-driven infiltration, semiconducting polymers, tunable electron affinity

Received: February 25, 2020

Revised: April 2, 2020

Published online:

- [1] B. D. Fahlman, *Semiconductors*, Springer Netherlands, Dordrecht **2018**, pp. 263–371.
- [2] H. Méndez, G. Heimel, A. Opitz, K. Sauer, P. Barkowski, M. Oehzelt, J. Soeda, T. Okamoto, J. Takeya, J. B. Arlin, J. Y. Balandier, Y. Geerts, N. Koch, I. Salzmann, *Angew. Chem.* **2013**, *52*, 7751.
- [3] A. C. Arias, J. D. MacKenzie, I. McCulloch, J. Rivnay, A. Salleo, *Chem. Rev.* **2010**, *110*, 3.
- [4] H. Ma, H.-L. Yip, F. Huang, A. K.-Y. Jen, *Adv. Funct. Mater.* **2010**, *20*, 1371.
- [5] D. T. Scholes, P. Y. Yee, J. R. Lindemuth, H. Kang, J. Onorato, R. Ghosh, C. K. Luscombe, F. C. Spano, S. H. Tolbert, B. J. Schwartz, *Adv. Funct. Mater.* **2017**, *27*, 1702654.
- [6] T. J. Aubry, J. C. Axtell, V. M. Basile, K. J. Winchell, J. R. Lindemuth, T. M. Porter, J. Liu, A. N. Alexandrova, C. P. Kubiak, S. H. Tolbert, A. M. Spokoyny, B. J. Schwartz, *Adv. Mater.* **2019**, *31*, 1805647.
- [7] A. R. Chew, R. Ghosh, Z. Shang, F. C. Spano, A. Salleo, *J. Phys. Chem. Lett.* **2017**, *8*, 4974.
- [8] R. Ghosh, A. R. Chew, J. Onorato, V. Pakhnyuk, C. K. Luscombe, A. Salleo, F. C. Spano, *J. Phys. Chem. C* **2018**, *122*, 18048.
- [9] R. Ghosh, C. K. Luscombe, M. Hamsch, S. C. B. Mannsfeld, A. Salleo, F. C. Spano, *Chem. Mater.* **2019**, *31*, 7033.
- [10] Q. Pei, G. Zuccarello, M. Ahlskog, O. Inganäs, *Polymer* **1994**, *35*, 1347.
- [11] J. D. Yuen, A. S. Dhoot, E. B. Namdas, N. E. Coates, M. Heeney, I. McCulloch, D. Moses, A. J. Heeger, *J. Am. Chem. Soc.* **2007**, *129*, 14367.
- [12] J. F. Chang, J. Clark, N. Zhao, H. Sirringhaus, D. W. Breiby, J. W. Andreasen, M. M. Nielsen, M. Giles, M. Heeney, I. McCulloch, *Phys. Rev. B - Condens. Matter Mater. Phys.* **2006**, *74*, 115318.
- [13] I. E. Jacobs, A. J. Moulé, *Adv. Mater.* **2017**, *29*, 1703063.
- [14] H. T. Nicolai, M. Kuik, G. A. H. Wetzelaer, B. de Boer, C. Campbell, C. Risko, J. L. Brédas, P. W. M. Blom, *Nat. Mater.* **2012**, *11*, 882.
- [15] L.-L. Chua, J. Zaumseil, J.-F. Chang, E. C.-W. Ou, P. K.-H. Ho, H. Sirringhaus, R. H. Friend, *Nature* **2005**, *434*, 194.
- [16] D. T. Scholes, S. A. Hawks, P. Y. Yee, H. Wu, J. R. Lindemuth, S. H. Tolbert, B. J. Schwartz, *J. Phys. Chem. Lett.* **2015**, *6*, 4786.
- [17] I. E. Jacobs, E. W. Aasen, J. L. Oliveira, T. N. Fonseca, J. D. Roehling, J. Li, G. Zhang, M. P. Augustine, M. Mascal, A. J. Moulé, *J. Mater. Chem. C* **2016**, *4*, 3454.
- [18] C. Y. Kao, B. Lee, L. S. Wielunski, M. Heeney, I. McCulloch, E. Garfunkel, L. C. Feldman, V. Podzorov, *Adv. Funct. Mater.* **2009**, *19*, 1906.
- [19] O. Khatib, B. Lee, J. Yuen, Z. Q. Li, M. Di Ventra, A. J. Heeger, V. Podzorov, D. N. Basov, *J. Appl. Phys.* **2010**, *107*, 12.
- [20] K. Kang, S. Watanabe, K. Broch, A. Sepe, A. Brown, I. Nasrallah, M. Nikolka, Z. Fei, M. Heeney, D. Matsumoto, K. Marumoto, H. Tanaka, S. I. Kuroda, H. Sirringhaus, *Nat. Mater.* **2016**, *15*, 896.
- [21] S. N. Patel, A. M. Gludell, K. A. Peterson, E. M. Thomas, K. A. O'Hara, E. Lim, M. L. Chabiny, *Sci. Adv.* **2017**, *3*, 24.
- [22] J. Hynynen, D. Kiefer, L. Yu, R. Kroon, R. Munir, A. Amassian, M. Kemerink, C. Müller, *Macromolecules* **2017**, *50*, 8140.
- [23] E. Lim, K. A. Peterson, G. M. Su, M. L. Chabiny, *Chem. Mater.* **2018**, *30*, 998.
- [24] M. T. Fontana, D. A. Stanfield, D. T. Scholes, K. J. Winchell, S. H. Tolbert, B. J. Schwartz, *J. Phys. Chem. C* **2019**, *123*, 22711.
- [25] A. Hamidi-Sakr, L. Biniek, J. L. Bantignies, D. Maurin, L. Herrmann, N. Leclerc, P. Lévêque, V. Vijayakumar, N. Zimmermann, M. Brinkmann, *Adv. Funct. Mater.* **2017**, *27*, 1700173.
- [26] V. Vijayakumar, Y. Zhong, V. Untilova, M. Bahri, L. Herrmann, L. Biniek, N. Leclerc, M. Brinkmann, *Adv. Energy Mater.* **2019**, *9*, 1900266.
- [27] V. Vijayakumar, E. Zaborova, L. Biniek, H. Zeng, L. Herrmann, A. Carvalho, O. Boyron, N. Leclerc, M. Brinkmann, *ACS Appl. Mater. Interfaces* **2019**, *11*, 4942.
- [28] J. Lindemuth, *Spie* **2012**, *8470*, 84700G.
- [29] F. Werner, *J. Appl. Phys.* **2017**, *122*, 13.
- [30] D. T. Scholes, P. Y. Yee, G. R. McKeown, S. Li, H. Kang, J. R. Lindemuth, X. Xia, S. C. King, D. S. Seferos, S. H. Tolbert, B. J. Schwartz, *Chem. Mater.* **2019**, *31*, 73.
- [31] Y. Chen, H. T. Yi, V. Podzorov, *Phys. Rev. Appl.* **2016**, *5*, 034008.
- [32] H. T. Yi, Y. N. Gartstein, V. Podzorov, *Sci. Rep.* **2016**, *6*, 23650.
- [33] X. Zhang, H. Bronstein, A. J. Kronemeijer, J. Smith, Y. Kim, R. J. Kline, L. J. Richter, T. D. Anthopoulos, H. Sirringhaus, K. Song, M. Heeney, W. Zhang, I. McCulloch, D. M. DeLongchamp, *Nat. Commun.* **2013**, *4*, 2238.
- [34] R. Noriega, J. Rivnay, K. Vandewal, F. P. V. Koch, N. Stingelin, P. Smith, M. F. Toney, A. Salleo, *Nat. Mater.* **2013**, *12*, 1038.
- [35] J. C. Axtell, L. M. A. Saleh, E. A. Qian, A. I. Wixtrom, A. M. Spokoyny, *Inorg. Chem.* **2018**, *57*, 2333.
- [36] M. S. Messina, J. C. Axtell, Y. Wang, P. Chong, A. I. Wixtrom, K. O. Kirlikovali, B. M. Upton, B. M. Hunter, O. S. Shafaat, S. I. Khan, J. R. Winkler, H. B. Gray, A. N. Alexandrova, H. D. Maynard, A. M. Spokoyny, *J. Am. Chem. Soc.* **2016**, *138*, 6952.
- [37] P. Pingel, R. Schwarzl, D. Neher, *Appl. Phys. Lett.* **2012**, *100*, 143303.
- [38] P. Pingel, D. Neher, *Phys. Rev. B* **2013**, *87*, 115209.
- [39] H. Tanaka, K. Kanahashi, N. Takekoshi, H. Mada, H. Ito, Y. Shimoi, H. Ohta, T. Takenobu, *Sci. Adv.* **2020**, *6*, eaay8065.
- [40] F. A. Larrain, C. Fuentes-Hernandez, W. F. Chou, V. A. Rodriguez-Toro, T. Y. Huang, M. F. Toney, B. Kippelen, *Energy Environ. Sci.* **2018**, *11*, 2216.
- [41] D. Kiefer, R. Kroon, A. I. Hofmann, H. Sun, X. Liu, A. Giovannitti, D. Stegerer, A. Cano, J. Hynynen, L. Yu, Y. Zhang, D. Nai,

- T. F. Harrelson, M. Sommer, A. J. Moulé, M. Kemerink, S. R. Marder, I. McCulloch, M. Fahlman, S. Fabiano, C. Müller, *Nat. Mater.* **2019**, *18*, 149.
- [42] Y. Karpov, N. Kiri, M. Al-Hussein, M. Hamsch, T. Beryozkina, V. Bakulev, S. C. Mannsfeld, B. Voit, A. Kiri, *Chem. Commun.* **2018**, *54*, 307.
- [43] R. Fujimoto, Y. Yamashita, S. Kumagai, J. Tsurumi, A. Hinderhofer, K. Broch, F. Schreiber, S. Watanabe, J. Takeya, *J. Mater. Chem. C* **2017**, *5*, 12023.
- [44] P. Y. Yee, D. T. Scholes, B. J. Schwartz, S. H. Tolbert, *J. Phys. Chem. Lett.* **2019**, *10*, 4929.
- [45] M. G. Voss, D. T. Scholes, J. R. Challa, B. J. Schwartz, *Faraday Discuss.* **2019**, *216*, 339.
- [46] Z. Liang, Y. Zhang, M. Souri, X. Luo, A. M. Boehm, R. Li, Y. Zhang, T. Wang, D. Y. Kim, J. Mei, S. R. Marder, K. R. Graham, *J. Mater. Chem. A* **2018**, *6*, 16495.
- [47] B. Nell, K. Ortstein, O. V. Boltalina, K. Vandewal, *J. Phys. Chem. C* **2018**, *122*, 11730.
- [48] J. Li, G. Zhang, D. M. Holm, I. E. Jacobs, B. Yin, P. Stroeve, M. Mascali, A. J. Moulé, *Chem. Mater.* **2015**, *27*, 5765.
- [49] B. Wegner, L. Grubert, C. Dennis, A. Opitz, A. Röttger, Y. Zhang, S. Barlow, S. R. Marder, S. Hecht, K. Müllen, N. Koch, *J. Mater. Chem. C* **2019**, *7*, 13839.
- [50] Y. Karpov, T. Erdmann, I. Raguzin, M. Al-Hussein, M. Binner, U. Lappan, M. Stamm, K. L. Gerasimov, T. Beryozkina, V. Bakulev, D. V. Anokhin, D. A. Ivanov, F. Günther, S. Gemming, G. Seifert, B. Voit, R. Di Pietro, A. Kiri, *Adv. Mater.* **2016**, *28*, 6003.
- [51] H. Méndez, G. Heimel, S. Winkler, J. Frisch, A. Opitz, K. Sauer, B. Wegner, M. Oehzelt, C. Röthel, S. Duhm, D. Többsen, N. Koch, I. Salzmann, *Nat. Commun.* **2015**, *6*, 8560.
- [52] A. I. Wixtrom, Y. Shao, D. Jung, C. W. Machan, S. N. Kevork, E. A. Qian, J. C. Axtell, S. I. Khan, C. P. Kubiak, A. M. Spokoyny, *Inorg. Chem. Front.* **2016**, *3*, 711.
- [53] A. I. Wixtrom, Z. A. Parvez, M. D. Savage, E. A. Qian, D. Jung, S. I. Khan, A. L. Rheingold, A. M. Spokoyny, *Chem. Commun.* **2018**, *54*, 5867.
- [54] C. Hansch, A. Leo, R. W. Taft, *Chem. Rev.* **1991**, *91*, 165.
- [55] P. G. Brown, H. Sirringhaus, M. Harrison, M. Shkunov, R. H. Friend, *Phys. Rev. B - Condens. Matter Mater. Phys.* **2001**, *63*, 125204.
- [56] J. L. Bredas, G. B. Street, *Acc. Chem. Res.* **1985**, *18*, 309.
- [57] J. Yamamoto, Y. Furukawa, *J. Phys. Chem. B* **2015**, *119*, 4788.
- [58] C. Wang, D. T. Duong, K. Vandewal, J. Rivnay, A. Salleo, *Phys. Rev. B - Condens. Matter Mater. Phys.* **2015**, *91*, 085205.
- [59] R. Ghosh, C. M. Pochas, F. C. Spano, *J. Phys. Chem. C* **2016**, *120*, 11394.
- [60] E. Lim, A. M. Gludell, R. Miller, M. L. Chabiny, *Adv. Electron. Mater.* **2019**, *5*, 1800915.
- [61] C. M. Pochas, F. C. Spano, *J. Chem. Phys.* **2014**, *140*, 24.
- [62] I. E. Jacobs, C. Cendra, T. F. Harrelson, Z. I. Bedolla-Valdez, R. Faller, A. Salleo, A. J. Moulé, *Mater. Horiz.* **2018**, *5*, 655.
- [63] B. Neelamraju, K. E. Watts, J. E. Pemberton, E. L. Ratcliff, *J. Phys. Chem. Lett.* **2018**, *9*, 6871.
- [64] J. E. Cochran, M. J. Junk, A. M. Gludell, P. L. Miller, J. S. Cowart, M. F. Toney, C. J. Hawker, B. F. Chmelka, M. L. Chabiny, *Macromolecules* **2014**, *47*, 6836.
- [65] E. M. Thomas, E. C. Davidson, R. Katsumata, R. A. Segalman, M. L. Chabiny, *ACS Macro Lett.* **2018**, *7*, 1492.
- [66] L. J. Van der Pauw, *Phys. Tech. Rev.* **1958**, *1958*, 220.
- [67] V. A. Kolesov, C. Fuentes-Hernandez, W. F. Chou, N. Aizawa, F. A. Larrain, M. Wang, A. Perrotta, S. Choi, S. Graham, G. C. Bazan, T. Q. Nguyen, S. R. Marder, B. Kippelen, *Nat. Mater.* **2017**, *16*, 474.
- [68] P. Reiser, L. Müller, V. Sivanesan, R. Lovrincic, S. Barlow, S. R. Marder, A. Pucci, W. Jaegermann, E. Mankel, S. Beck, *J. Phys. Chem. C* **2018**, *122*, 14518.
- [69] N. C. Miller, E. Cho, R. Gysel, C. Risko, V. Coropceanu, C. E. Miller, S. Sweetnam, A. Sellinger, M. Heeney, I. McCulloch, J.-L. Brédas, M. F. Toney, M. D. McGehee, *Adv. Energy Mater.* **2012**, *2*, 1208.
- [70] J. K. Keum, J. F. Browning, K. Xiao, M. Shao, C. E. Halbert, K. Hong, *Appl. Phys. Lett.* **2013**, *103*, 3.
- [71] S. B. Kirschner, N. P. Smith, K. A. Wepasnick, H. E. Katz, B. J. Kirby, J. A. Borchers, D. H. Reich, *J. Mater. Chem.* **2012**, *22*, 4364.
- [72] K. H. Lee, Y. Zhang, P. L. Burn, I. R. Gentle, M. James, A. Nelson, P. Meredith, *J. Mater. Chem. C* **2013**, *1*, 2593.
- [73] A. Andersson, *Solid State Ionics* **2000**, *130*, 41.
- [74] E. Meulenkaamp, *Solid State Ionics* **1999**, *126*, 235.
- [75] G. M. Newbloom, K. M. Weigandt, D. C. Pozzo, *Soft Matter* **2012**, *8*, 8854.
- [76] E. D. Miller, M. L. Jones, M. M. Henry, P. Chery, K. Miller, E. Jankowski, *Polymers* **2018**, *10*, 1305.
- [77] J. H. Burke, M. J. Bird, *Adv. Mater.* **2019**, *31*, 1806863.
- [78] L. Zhu, E. G. Kim, Y. Yi, J. L. Brédas, *Chem. Mater.* **2011**, *23*, 5149.
- [79] I. Salzmann, G. Heimel, M. Oehzelt, S. Winkler, N. Koch, *Acc. Chem. Res.* **2016**, *49*, 370.